Physica B 721 (2026) 418050

Contents lists available at ScienceDirect

Physica B: Condensed Matter

journal homepage: www.elsevier.com/locate/physb

Cold plasma-synthesized carbon quantum dots for enhanced photovoltaic performance in quantum dot-sensitized solar cells

W.I. Sandamali [a,b,c,*], G.K.R. Senadeera [a,b], Janith Weerasinghe [d], V.P.S. Perera [a], M.A.K.L. Dissanayake [b]

[a] Department of Physics, The Open University of Sri Lanka, Nawala, Nugegoda, 10250, Sri Lanka
[b] National Institute of Fundamental Studies, Hantana Road, Kandy, 20000, Sri Lanka
[c] Department of Materials Technology, Rajarata University of Sri Lanka, Mihintale, 50300, Sri Lanka
[d] School of Engineering, The Australian National University, Canberra, ACT, 2600, Australia

ARTICLE INFO

Keywords:
Carbon quantum dots
CQD
TiO_2/CdS photoanode
CdS QDSSC
Quantum dot sensitized solar cells

ABSTRACT

The effect on the photovoltaic properties of the TiO_2-based cadmium sulfide (CdS) quantum dot sensitized solar cells (QDSSCs) was investigated by incorporating carbon quantum dots (CQDs) synthesized via a cold atmospheric plasma method. CQD incorporated photoanodes were characterized by SEM, TEM, XRD, Raman spectroscopy, FTIR spectroscopy, PL spectroscopy, UV–visible spectroscopy, and Mott-Schottky techniques. TEM measurements revealed that the CQDs were mostly spherical with an average diameter of ~3 nm. The presence of CQDs in the TiO_2 photoanode was confirmed by both Raman spectroscopy and FTIR measurements. The findings from the PL and IPCE analyses showed that CQDs functioned as an energy down-converting material, broadening the responsive range of the CdS QDSSC to encompass higher energy photons. QDSSCs fabricated with CQDs-incorporated photoanode, a sulfide redox couple, and a Pt counter electrode exhibited a 31.3 % enhancement in power conversion efficiency, leading to a 1.68 % efficiency compared to the 1.28 % efficiency of the pristine TiO_2 photoanode.

1. Introduction

Quantum dot sensitized solar cells (QDSSCs) are a class of photovoltaic devices belonging to the third generation of solar cells, targeting higher power conversion efficiencies (PCEs) and cost effectiveness [1–3]. QDSSCs employ quantum dots (QDs) as the active light harvester. Quantum dots are zero-dimensional, semiconducting nanocrystals with many interesting optoelectronic features, such as multiple exciton generation, tunable bandgaps, high molar extinction coefficients, etc. [4–6]. QDSSCs strategically utilize the QDs' ability to produce electron-hole pairs upon light illumination for active photocurrent generation. According to the National Renewable Energy Laboratory (NREL) database, quantum dot solar cells currently have a best research cell efficiency of 19.1 % [7]. QDSSCs reportedly present a much higher theoretical efficiency limit, surpassing the Shockley-Queisser limitation of single junction solar cells [3,8,9]. Hence, QDSSCs have a great potential for highly efficient photovoltaics with continued research.

A typical QDSSC is composed of a photoanode, a counter electrode (CE), and an electrolyte layer between these two electrodes. Photoanodes are usually developed with a film of wide bandgap semiconductor (e.g., TiO_2, ZnO, SnO_2, etc.), which is sensitized with low bandgap QDs (e.g., CdS, PbS, CdSe, etc.) [5,6]. CEs such as CuS, Pt, PbS, and carbon-based materials are largely employed in QDSSCs [6,10]. The electrolytes can be in the liquid, semi-solid, or solid forms. Polysulfide is a popular choice of electrolytes in QDSSCs [6,11]. There are many ongoing research studies related to different components of QDSSCs, including pursuing novel materials, interfacial engineering, and new technological adaptations [5,6,11]. When photoanodes are considered, flaws such as limited electron generation, higher charge recombination losses, and insufficient stability need to be addressed to achieve satisfactory performance [5,12,13]. Nano structuring, passivation layers, core-shell structures, co-sensitization, doping, incorporating light scattering materials, etc., are some strategies adopted for these purposes [5,6,13,14]. The present study investigates the incorporation of carbon quantum dots (CQDs) in the TiO_2 photoanode as a strategy to enhance the photovoltaic performance of CdS QDSSCs by boosting photocurrent generation in the photoanode.

Zero-dimensional (0 D) carbon nanomaterials, such as carbon

* Corresponding author. Department of Physics, The Open University of Sri Lanka, Nawala, Nugegoda, 10250, Sri Lanka.
E-mail address: isharas@tec.rjt.ac.lk (W.I. Sandamali).

https://doi.org/10.1016/j.physb.2025.418050
Received 10 September 2025; Received in revised form 4 November 2025; Accepted 12 November 2025
Available online 14 November 2025

quantum dots (CQDs) and graphene quantum dots (GQDs), have gained recognition for their adaptability and impressive characteristics, including tunable optical properties, fluorescence, electroluminescence, up-conversion photoluminescence, chemical inertness, thermal stability, electrical conductivity, facile surface functionalization, nontoxicity, biocompatibility, etc. [15–17]. CQDs were first discovered by Xu et al., in 2004 while purifying single-walled carbon nanotubes (SWNTs) [18,19]. Numerous studies conducted since then have demonstrated their tremendous potential across a broad range of disciplines, including energy conversion, energy storage, optoelectronics, catalysis, electrochemical, optical, and biosensors, bioimaging, drug delivery, and environmental remediation [15,19–23]. CQDs usually appear as spherical, rod-like, or irregular structures less than 10 nm in size. Their properties could be tailored with surface modifications and doping by controlling the synthesis techniques, conditions, and precursors accordingly. CQDs often contain both crystalline and amorphous regions, with a center region mostly composed of sp^2-hybridized graphitic structures [20,22,24]. CQDs could be synthesized via both top-down and bottom-up routes. Top-down techniques, such as arc discharge, laser ablation, electrochemical oxidation, etc., involve chemical or physical breakdown of larger structures to obtain CQDs. Controlling the size and morphology of CQDs synthesized from these methods could be challenging. On the other hand, bottom-up techniques, such as pyrolysis, microwave synthesis, hydrothermal/solvothermal synthesis, template-based synthesis, etc., create CQDs starting from small molecular precursors, giving better control over their size, shape, and surface chemistry [16,20,25].

CQDs have a high potential for photovoltaic applications, such as QDSSCs [26–28], dye sensitized solar cells [29–31], organic solar cells [32,33], perovskite solar cells [34,35], Si junction solar cells [36], etc., due to their excellent optoelectronic properties. CQDs are not only capable of acting as sensitizers and co-sensitizers, they also can behave as dopants, donors, acceptors, charge transport materials, energy down-shift materials, etc., in these settings [24,37]. According to the literature, the current highest PCE for the CQD mono-sensitized QDSSCs is 1.36 % by Riaz et al. for N and S co-doped CQD sensitizers [26,27,38,39]. Additionally, there were few records of studies related to the incorporation of CQDs in CdS QDSSCs similar to the present study [40,41]. According to Zhao et al., the incorporation of Er-doped CQDs in TiO_2/CdS photoanodes led to widening of the light absorption range and speedy electron transport. They achieved 0.59 % PCE by constructing QDSSCs with these photoanodes and polysulfide electrolyte and Cu_2S CE, a far greater value than the 0.34 % of the devices without CQDs. Here, the Er-doped CQDs were synthesized by backflow and hydrothermal methods using triethylenetetramine hexaacetic acid as the precursor and erbium oxide as the dopant, and the technique for CQDs incorporation was immersing TiO_2 photoanodes in aqueous Er CQDs solution [41]. Another investigation by Huang et al. reported that the N-doped CQD incorporation improved the PCE of CdS QDSSCs up to 0.606 % from 0.430 %. The N-doped CQDs were synthesized by the hydrothermal method using cotton fiber as the precursor and urea as the dopant, and the CQD incorporation in TiO_2 photoanodes was achieved by immersing them in the CQD solution for 24 h [40]. In contrast to these studies, the present study explores a different route for both synthesis and incorporation of CQD in the photoanode. Here, CQDs are mixed with TiO_2 paste before fabricating the TiO_2 layer, instead of dipping already prepared TiO_2 photoanodes in CQD solutions as in the literature.

Moreover, the CQDs employed in this study were synthesized from 1,3,6,8-pyrenetetrasulfonic acid tetrasodium salt hydrate (PTSA) using a cold atmospheric plasma method [42]. In essence, plasma is an ionized gas made up of ions, electrons, reactive species, atoms, photons, and other elements. It is regarded as the fourth state of matter [43,44]. Plasma-based technologies are gaining popularity for the synthesis of nanomaterials because of their adaptable, cost-effective, and environmentally friendly nature [43,45]. Cold plasmas generated at ambient temperature and pressure are particularly advantageous as they do not necessitate costly and sophisticated instruments [42,43]. The present study includes a detailed analysis of the performance of cold atmospheric plasma synthesized CQD incorporated TiO_2/CdS photoanodes, and the corresponding QDSSCs fabricated by assembling with Pt CE and polysulfide electrolyte.

2. Materials and methods

2.1. Materials used

1,3,6,8-pyrenetetrasulfonic acid tetrasodium salt hydrate (PTSA), cadmium (II) chloride (99.99 %, Sigma Aldrich), fluorine doped tin oxide (FTO) coated glass (7 Ω cm^{-2}, Solaronix), methanol (99.8 %, Sigma Aldrich), nitic acid (70 %, Sigma-Aldrich), polyethylene glycol (99.8 %, Sigma Aldrich), potassium chloride (99 %, Aldrich), sodium sulfide hydrate (>60 %, Sigma Aldrich), sulfur (99 %, Daejng), titanium dioxide P25 powder (Degussa), titanium dioxide P90 powder (Evonik), and Triton X-100 (Sigma Aldrich) were used as received without any purification.

2.2. Synthesis of CQD

CQDs were synthesized according to a procedure reported by Weerasinghe et al. [42]. First, 6 g of 1,3,6,8-pyrenetetrasulfonic acid tetrasodium salt hydrate was dissolved in 100 mL of ultra-pure water. The prepared solution was placed under the plasma nozzle of an atmospheric air plasma system (Nanjing Suman Plasma Technology Model PG-1000 Z/E) connected to an air pump unit (Nanjing Suman Plasma Technology Model FP-290). The solution was treated with plasma for 10 min, with a continuous atmospheric air flow of 240 L min^{-1} in the system. Then, the solution was dialyzed to remove large particles and unreacted materials [42].

2.3. Fabrication of photoanodes

TiO_2 photoanodes were fabricated by developing two layers of TiO_2 P90 and a single layer of TiO_2 P25 on well-cleaned FTO glass substrates. The TiO_2 P90 layers were fabricated by spin coating a paste prepared by grinding 0.25 g of TiO_2 P90 with 1 ml of 0.1 M nitric acid (HNO_3), at 3000 rpm for 1 min. This was followed by sintering at 450 °C for 45 min in a muffle furnace. Then, a layer of TiO_2 P25 was constructed on top of TiO_2 P90 using the doctor blade method. For this, a paste was prepared by grinding 0.25 g of TiO_2 P25 with 1 drop of Triton-X 100 (~50 μl), 1 drop of PEG (~50 μl), and 1 ml of 0.1 M HNO_3. In the case of CQD incorporated photoanodes, different amounts (25–100 μl) of CQD solution (0.02 w/v%) were added to the TiO_2 P25 paste. Then, the doctor-bladed photoanodes were sintered at 450 °C for 45 min. Obtained TiO_2 photoanodes were sized to get an active surface area of ~0.16 cm^{-2}, followed by sensitization with CdS quantum dots using the successive ionic layer adsorption and reaction (SILAR) method. For this, 10 repeated cycles of dipping in 0.1 M $CdCl_2$ (aq), washing with distilled water, dipping in 0.1 M Na_2S (aq), washing, and drying were conducted. The CdS sensitized photoanodes were finally dried at 100 °C [46].

2.4. Fabrication of QDSSCs

The CdS QDSSCs were prepared by clipping developed photoanodes with a Pt CE and injecting polysulfide electrolyte in between them. The polysulfide electrolyte was prepared with sulfur (2 M), Na_2S (0.5 M), and KCl (0.2 M) in a mixture of deionized water and methanol in the ratio of 3:7 (v/v) [46].

2.5. Material characterization

Morphological studies of photoanodes were carried out with

Scanning Electron Microscopy (SEM) images (ZEISS EVO), and the CQDs and the photoanode materials were also analyzed with Transmission Electron Microscopy (TEM) images (AJEOL 2100 TEM). Structural analysis of photoanode materials was conducted by X-ray diffraction (XRD) data obtained from a Bruker D8 advanced eco X-ray diffraction system with Cu Kα radiation (λ = 1.54060 Å). A Raman spectroscopy analysis was conducted with a Renishaw basis Raman microscope operated with 514 nm lasers. Surface of the CQD incorporated photoanode was examined by Thermo Scientific TM ESCALAB Xi + X-ray photoelectron spectrometer (XPS). Attenuated total reflection infrared (ATR-IR) spectra of the photoanode materials were recorded using a Nicolet iS50 (Thermo Scientific) FTIR instrument. Optical absorption spectra were recorded using a Shimadzu 2450 UV–Vis spectrophotometer. The photoluminescence (PL) emission spectra were recorded using a HORIBA Duetta spectrofluorometer. Mott-Schottky measurements were taken with a three-electrode setup comprising a photoanode (working electrode), a Pt wire (CE), an Ag/AgCl standard reference electrode, and 0.05 M aqueous Na_2SO_4 electrolyte, using a Zahner Zennium electrochemical workstation at a frequency of 1.0 kHz.

2.6. Device characterization

Current density-voltage (*J-V*) characterizations of QDSSCs were carried out under simulated sunlight (100 mW cm^{-2}, AM1.5), using an Oriel Newport LCS-100 solar simulator and a Metrohm Autolab potentiostat/galvanostat. The incident photon-to current conversion efficiency (IPCE) measurements were conducted using a PVE300 photovoltaic QE system with a TMC 300 monochromator. Electrochemical Impedance Spectroscopy (EIS) analysis of the QDSSCs was performed using a Zahner Zennium electrochemical workstation.

3. Results and discussion

3.1. Morphological and structural characteristics of CQD and TiO_2 photoanodes

Fig. 1 (a) shows a photograph of the CQD incorporated TiO_2 photoanode (TiO_2/CQD), while Fig. 1 (c) shows a surface SEM image of the same photoanode. Meanwhile, Fig. 1 (b) and (d) show a photograph and a surface SEM image of the TiO_2 photoanode taken in a similar setting. TiO_2/CQD photoanodes appeared off-white compared to the bright white color of pristine TiO_2 photoanodes. According to Fig. 1(c) and (d), the agglomeration of particles in the TiO_2/CQD photoanode appears to be higher, potentially resulting in a rise in the surface roughness of the electrode [47]. However, significant changes were not observed in TiO_2 particles due to this incorporation of CQD, when examined under higher magnification.

Further characterization of the CQDs and TiO_2/CQD photoanode materials was carried out with Transmission Electron Microscopy (TEM) images and Image-*J* software. It was realized that the CQDs were mostly spherical with an average diameter of ~3 nm, from the TEM image of CQDs in Fig. 2 (a). The interplanar (*d*) spacing value of CQDs estimated from the visible lattice fringes in the image was 0.24 nm, which could be attributed to the (1120) lattice plane of graphene structures, respectively [26,30,42]. Fig. 2 (b) shows a TEM image of TiO_2/CQD photoanode materials. CQDs are marked with dashed circles in these images.

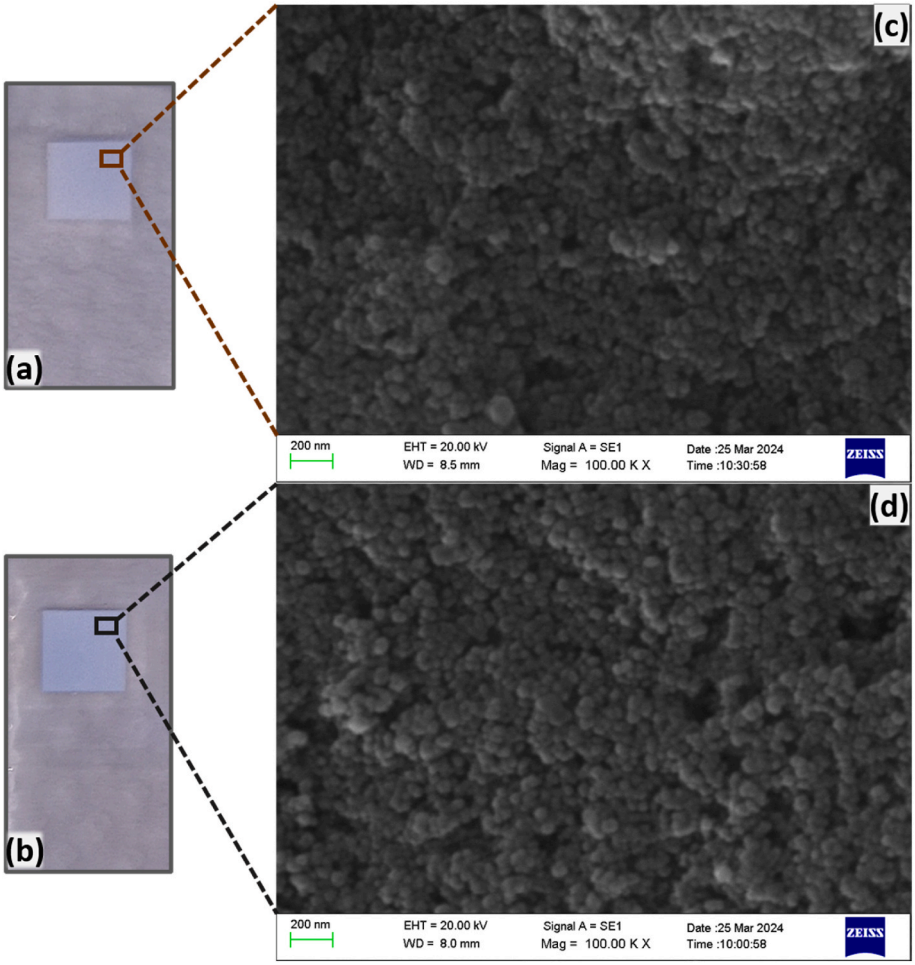

Fig. 1. Photographs of (a) TiO_2/CQD and (b) TiO_2 photoanodes, and SEM images of (c) TiO_2/CQD and (d) TiO_2 photoanodes.

According to this analysis, the sizes of TiO_2 nanoparticles were much larger (>20 nm) compared to CQDs (~3 nm). The *d*-spacing values estimated from visible lattice fringes in Fig. 2 (b) were 0.35 and 0.33 nm, which could be attributed to (101) lattice planes of anatase and (110) lattice planes of rutile TiO_2, respectively [48].

3.2. XRD, Raman, and XPS analysis of TiO_2 photoanodes

The X-ray diffraction (XRD) analysis of TiO_2 and TiO_2/CQD photoanode materials was carried out to identify any structural changes due to the incorporation of CQDs. These XRD patterns are displayed in Fig. 3, together with reference patterns for anatase and rutile crystal phases of TiO_2 [49]. The set of XRD peaks detected from both TiO_2 and TiO_2/CQD XRD patterns closely resembled each other, with no apparent diffraction from CQDs, as evident from Fig. 3. This could be due to overlapping with TiO_2 peaks or amorphous nature, and extremely low percentage of CQDs present in the mixture compared to TiO_2 [50–52]. In TiO_2, both anatase (AMCSD 0011765) and rutile (AMCSD 0011762) phases have tetragonal crystal structures; however, anatase belongs to the space group $I4_1/amd$ (141), whereas rutile belongs to the space group $P4_2/mnm$ (136) [49,53]. The presence of both anatase and rutile phases of TiO_2 in the analyzed materials was confirmed by comparing with the corresponding reference patterns. XRD peaks identified around 25.3°, 37.0°, 37.9°, 38.6°, 48.0°, 54.0°, 55.1°, 62.8°, 69.0°, and 70.2° angular positions in both patterns correspond to (101), (103), (004), (112), (200), (105), (211), (204), (116), and (220) crystal planes of anatase TiO_2 structure, respectively. Meanwhile, XRD peaks identified around 27.4°, 36.0°, 41.3°, 44.0°, 54.2°, 56.6°, 64.0°, 69.0°, and 75.1° angular positions in both patterns correspond to (110), (101), (111), (210), (211), (220), (310), (301), and (215) crystal planes of rutile TiO_2 structure, respectively [49,54]. The weight fraction of the anatase phase in the analyzed materials was determined from the following relation proposed by Spurr and Myers,

$$f = \frac{1}{1 + 1.26\frac{I_R}{I_A}} \quad (1)$$

where f is the weight fraction of anatase, I_A and I_R are the intensity of the strongest reflections of respective anatase and rutile phases [55]. The strongest reflection of the anatase phase was observed with the (101) crystal plane, while for the rutile phase it was with the (110) crystal plane. By substituting respective intensities of these peaks in the above relation, the weight percentage of the anatase phases in TiO_2 and TiO_2/CQD XRD was determined as 79.8 % and 79.6 %, respectively. Thus, these materials were predominantly in the anatase phase. Additionally, the inter-planar distances (d) and the average crystallite sizes (L) for the lattice planes of anatase (101) and rutile (110) of these materials were estimated from the Bragg and Scherrer equations mentioned below.

$$n\lambda = 2d\sin\theta \quad (2)$$

$$L = \frac{K\lambda}{\beta \cos\theta} \quad (3)$$

where n is the order of diffraction, λ is the wavelength (CuKα1 - 0.15406 nm) of the X-ray source, d is the inter-planar distance between lattice planes, θ is the Bragg angle, L is the average crystallite size, K is the shape factor (0.9), and β is the full-width half maximum (FWHM) of the diffraction peak (in radians) [53,56]. The estimated *d*-spacing and average crystallite sizes are tabulated in Table 1. The respective *d*-spacing values of anatase (101) and rutile (110) planes were 0.35 and 0.33 nm for both TiO_2 and TiO_2/CQD. This agrees with the *d*-spacing values estimated from the previous TEM analysis (Fig. 2). The average crystallite sizes calculated for anatase (101) planes for TiO_2 and TiO_2/CQD were 22.46 and 22.50 nm, respectively. Meanwhile, the average crystallite sizes calculated for rutile (110) planes for TiO_2 and TiO_2/CQD were 31.19 and 31.50 nm, respectively. Thus, no significant alterations in the TiO_2 crystal structures or phases were detected as a result of the CQD incorporation.

Raman spectroscopy is a popular technique for carbon-related

Table 1
Calculated crystallographic parameters for TiO_2 and TiO_2/CQD.

	Anatase (101)			Rutile (110)		
	2θ	d-spacing (nm)	L (nm)	2θ	d-spacing (nm)	L (nm)
TiO_2	25.27	0.35	22.46	27.41	0.33	31.19
TiO_2/CQD	25.27	0.35	22.50	27.40	0.33	31.50

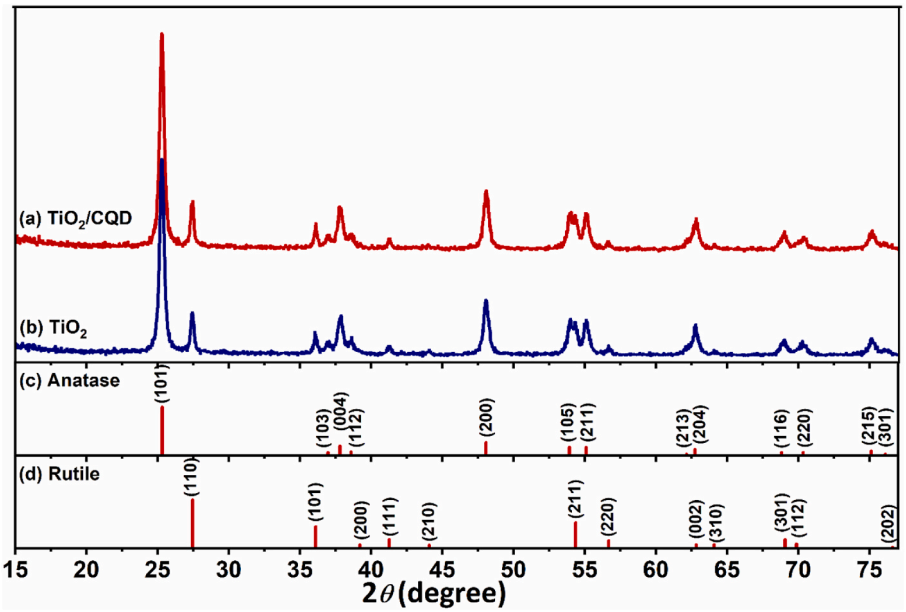

Fig. 3. XRD patterns of (a) TiO_2/CQD, (b) TiO_2, and reference patterns of (c) anatase and (d) rutile TiO_2 [49,54].

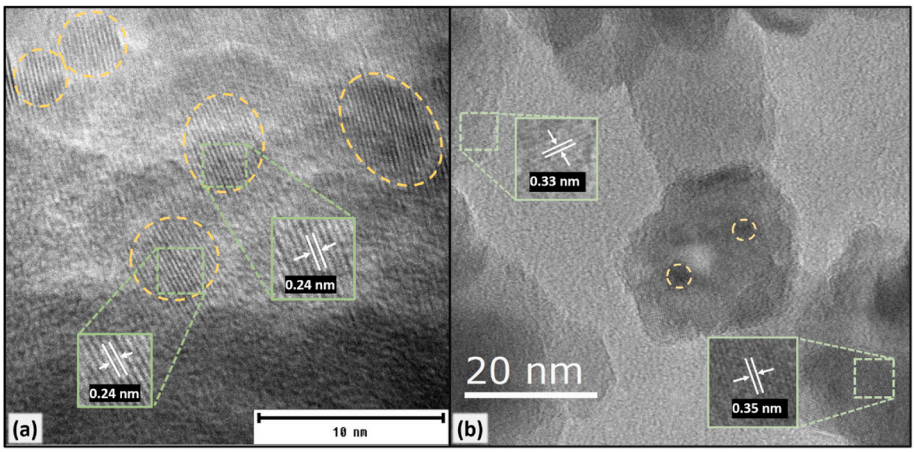

Fig. 2. TEM images of (a) CQD and (b) TiO_2/CQD photoanode materials.

material analysis due to its high sensitivity towards carbon materials [57]. Fig. 4 shows the Raman spectra of (a) TiO_2, (b) TiO_2/CQD, and (c) CQD. It is well understood that graphitic carbon structures, in particular, could be evaluated from two characteristic Raman bands, which often appear around 1350 cm^{-1} (*D* band) and 1580 cm^{-1} (*G* band) [58,59]. The *G* band results from in-plane stretching E_{2g} symmetrical mode vibrations of sp^2 carbon atoms, while the *D* band results from defect and disorder-activated A_{1g} symmetrical mode vibrations in the hexagonal aromatic ring [60–62]. Meanwhile, bands characteristic of both anatase and rutile TiO_2 phases could be detected from the Raman spectra; thus, it can also be utilized as a tool for investigating TiO_2 structures [63]. Fig. 4 (c) shows the Raman spectrum acquired for CQDs. The bands around 1212 cm^{-1} could be from the molecular vibrations from sp^3 carbon bonds [64,65]. The dominant bands around 1339 and 1623 cm^{-1} were identified as the usual *D* and *G* bands of carbon structures. The shifting and widening of the bands could be a result of overlapping Raman bands due to various defects and functional groups present in CQDs [59,62,65,66]. Raman spectra acquired for TiO_2 and TiO_2/CQD photoanode surfaces are shown in Fig. 4(a) and (b). Raman bands observed around 145, 199, 399, 520, and 640 cm^{-1} were attributed to the E_g, E_g, B_{1g}, A_{1g} and/or B_{1g}, and E_g vibrational modes of anatase TiO_2, and the Raman band observed around 445 cm^{-1} was attributed to the E_g vibrational mode of rutile TiO_2 in both of these spectra [63,67]. Due to highly intense Raman bands of anatase TiO_2 and a much larger proportion of TiO_2 in the system, Raman bands of CQDs were difficult to distinguish from the given scale. Hence, the 1000-1850 cm^{-1} region in each spectrum was enlarged and shown as insets in Fig. 4(a) and (b). The presence of CQDs in the TiO_2/CQD photoanode was confirmed by the appearance

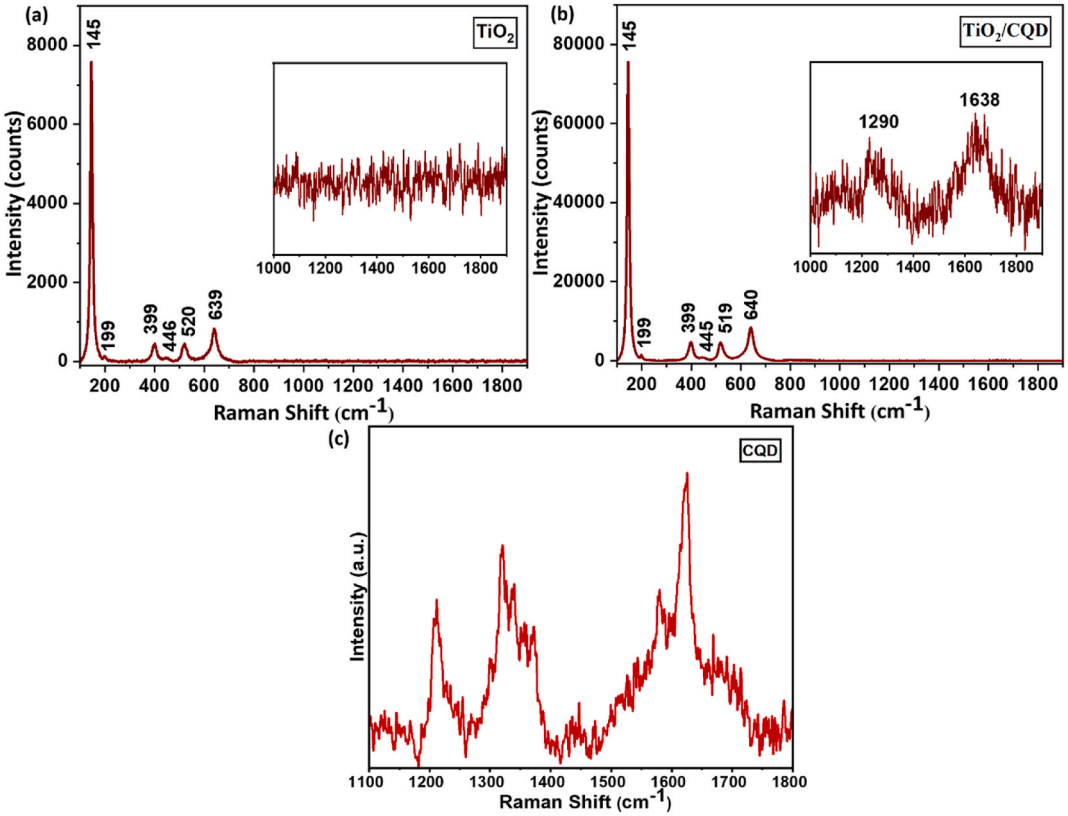

Fig. 4. Raman spectra of (a) TiO_2, (b) TiO_2/CQD, and (c) CQD.

of Raman bands around 1290 and 1638 cm^{-1}, corresponding to the *D* and *G* band regions of CQDs, whereas such bands were not present in the TiO_2 spectrum. Another interesting observation from these spectra was the higher intensity (no. of counts) of the Raman bands in the TiO_2/CQD photoanode compared to the normal photoanode. This was likely due to an amplification of Raman signals influenced by CQDs. Thus, the CQDs employed in this study have potential for future applications similar to graphene-enhanced Raman scattering (GERS) and surface-enhanced Raman spectroscopy (SERS) [68–70].

X-ray Photoelectron spectroscopy (XPS) was performed to identify the potential chemical states and the elements on the TiO_2/CQD photoanode surface [71,72]. According to the extracted data, the primary elements present on the photoanode surface were C, Ti, and O, with their respective atomic compositions around 23.74 %, 24.14 %, and 52.12 %. The full XPS survey and the high-resolution scans of C 1s, Ti 2p, and O 1s are displayed in Fig. 5(d)–(a), (b), and (c), respectively [73]. The XPS peaks detected from the deconvoluted high-resolution C 1s scan (Fig. 5 (a)) were assigned to C bonded as C sp^2 (284.4 eV), C sp^3 (284.8 eV), C–O (286.0 eV), and C=O (288.2 eV) [66,74–77]. These responses could be a result of CQDs in the photoanode and residual products from carbon-containing additives used in TiO_2 paste preparation. Additionally, three XPS peaks were identified from the deconvoluted high-resolution O 1s spectrum (Fig. 5 (c)), and they were assigned to O bonded as O-Ti (529.5 eV), O-C/O=C (530.0 eV), and O-H (531.3 eV) [26,72,76]. These responses could be resulting from TiO_2, oxygen-containing functional groups in CQDs, residual materials, and adsorbed H_2O. The two prominent peaks observed in the deconvoluted Ti 2p spectrum (Fig. 5 (b)) were assigned to the spin-orbit doublet of Ti^{4+} with a characteristic splitting energy of 5.7 eV: Ti^{4+} $2p_{3/2}$ (458.4 eV) and Ti^{4+} $2p_{1/2}$ (464.1 eV). In addition, the much smaller peak around 458.1 eV (Ti^{3+} $2p_{1/2}$) was assigned to defect-related Ti^{3+} in the TiO_2 lattice [72,78,79].

3.3. FTIR and UV–visible absorption analysis of CQD and TiO_2 photoanodes

Attenuated Total Reflection Fourier Transform Infrared (ATR-FTIR) spectroscopy is a convenient technique with minimum sample preparation, ideal for identifying chemical bonds and surface functional groups based on the IR-induced molecular vibrations [80,81]. The ATR-FTIR spectra recorded for CQDs, TiO_2, and TiO_2/CQD materials are displayed in Fig. 6. The vibrational bands observed around 2360 and 2342 cm^{-1} in all three spectra are characteristic of the atmospheric CO_2 [82]. The band observed around 3642 and the broad band around 3362 cm^{-1} in the CQD spectra could be attributed to the stretching vibrations of O-H bonds, while the band around 2907 cm^{-1} could be attributed to the stretching of C-H [27,30]. The sharp band appearing around 1647 cm^{-1} could be a combined effect of stretching of C=C, C=O, and C=N bonds, and bending of N-H bonds [31,82,83]. The FTIR band around 1497 cm^{-1} could be assigned to bending of C-H bonds, while the band around 1362 cm^{-1} could arise from bending of O-H, bending and deformation of C-H, and stretching of S=O bonds [84–86]. The vibrational band around 1202 cm^{-1} could be attributed to C-H wagging and stretching vibrations of C-O and C-N bonds, while the band around 657 cm^{-1} could be a result of bending of C-H bonds [84,87,88]. In the FTIR spectrum of TiO_2, a broad band was observed around 3373 cm^{-1} due to stretching vibrations of O-H bonds. Other FTIR bands observed around 1710, 1653, 1559, 1399, 1300, 1100, and 649 cm^{-1} could be assigned to C=O stretching, C=C stretching, O-H bending in absorbed hydroxyl groups, O-H bending, C-O stretching, and C-O stretching, respectively [89–91]. The influence of functional groups in CQDs was apparent in the FTIR spectrum of TiO_2/CQD, when compared with the FTIR spectrum of TiO_2. Notably, a higher band intensity around 1705 and 1221 cm^{-1} regions in the FTIR spectrum of TiO_2/CQD was observed, indicating the presence of additional vibrational bands from CQDs around 1647 and 1202 cm^{-1} regions.

The optical absorption of photovoltaic materials is a critical

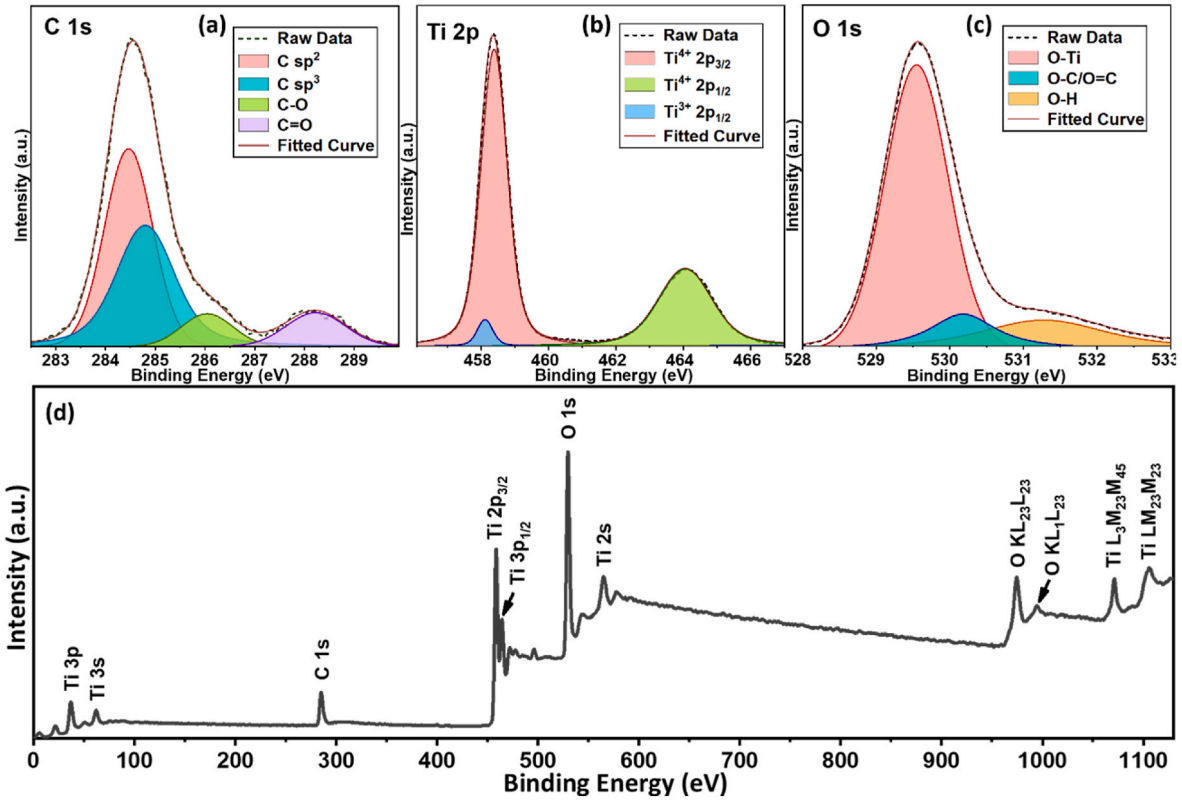

Fig. 5. XPS spectra of (a) C 1s, (b) Ti 2p, (c) O 1s, and (d) full scans.

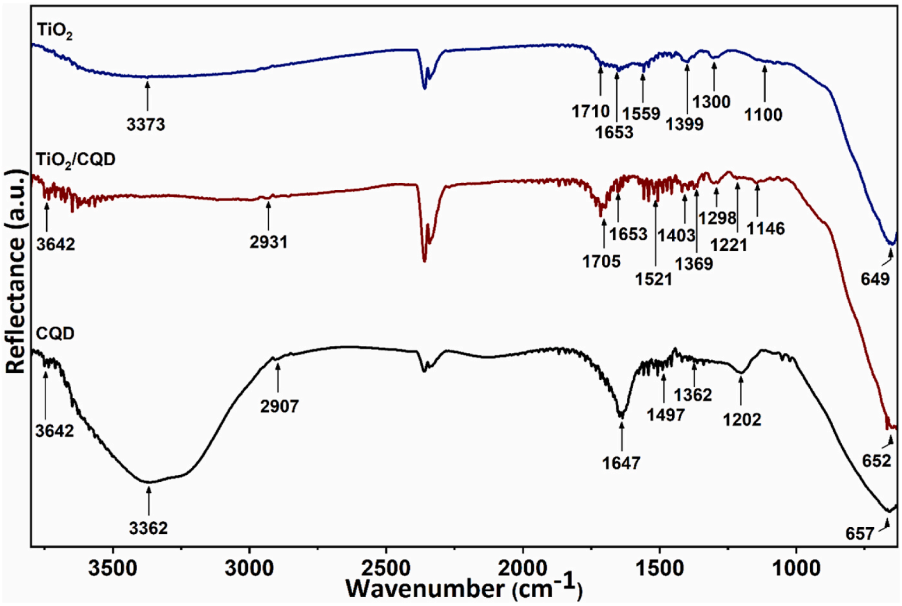

Fig. 6. FTIR spectra of CQD, TiO_2/CQD, and TiO_2.

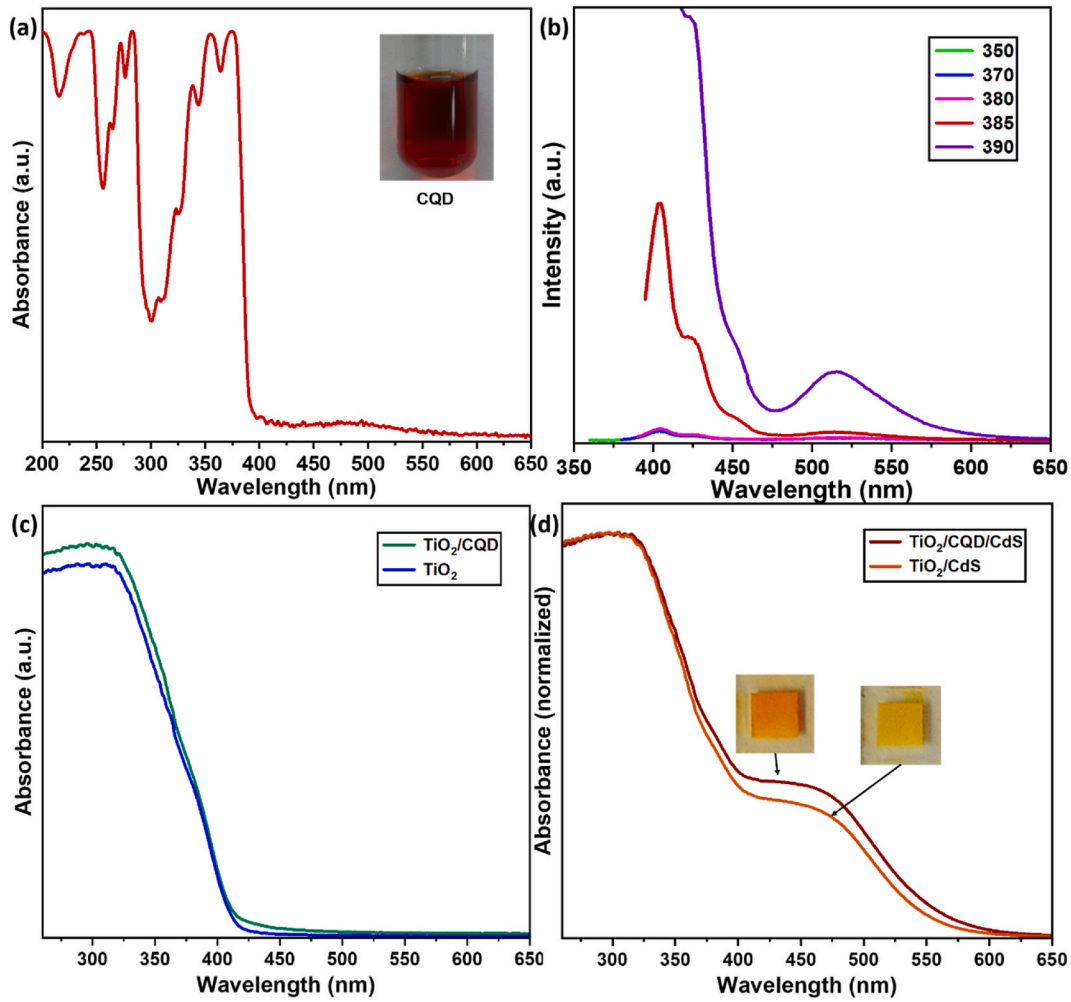

Fig. 7. (a) UV–visible spectra of CQD, (b) PL emission spectra of CQD, and UV–visible spectra of (c) TiO_2, TiO_2/CQD photoanodes and (d) TiO_2/CdS, TiO_2/CQD/CdS photoanodes.

parameter for the operation of QDSSCs. Hence, the optical properties of the CQDs and prepared TiO_2 photoanodes were evaluated from their UV–visible spectra displayed in Fig. 7. The optical behavior of CQDs was further evaluated using the photoluminescence (PL) emission spectra of CQDs, as shown in Fig. 7 (b). The absorptions related to electronic transitions in the core and edge regions, and the surface states are usually noticeable in the UV–visible spectra of CQDs [24,27]. Four main absorption regions were identified around 240 nm, 270 nm, 350 nm, and 480 nm in the UV–visible spectrum of CQD in the present study (Fig. 7 (a)), which could be resulting from π-π* transition of aromatic sp^2 carbons, n-π* transition of C=N bonds, n-π* transition of C=O bonds, and electronic transitions of various surface states and functional groups, respectively [31,92–94]. The PL emission spectra of CQDs were recorded by exciting with higher energy photons in the range of 350–390 nm, as shown in Fig. 7 (b). According to these spectra, the emission from excited CQDs occurred in the 370–650 nm range with a peak emission around 405 nm. Additionally, the emission peaked around 425, 450, and 515 nm. When increasing the excitation wavelength, the intensity of the emission spectrum also increased; however, the pattern of the emission spectra was maintained. When the CQDs were excited with higher energy photons in the UV region, the resulting emission was with lower energy, spreading towards the visible region. Thus, the PL emission spectra show the energy down conversion capability of CQDs [30,95]. Fig. 7 (c) and (d) show UV–visible spectra of TiO_2 and TiO_2/CQD photoanodes, which were recorded before and after sensitizing with CdS QDs. As evident from these spectra, TiO_2 shows a strong absorption in the region <400 nm, while CdS QDs show a strong absorption in the 400–600 nm region, with an absorbance edge around 460 nm. A slight increase in absorbance in the 410–490 nm region was observed due to the incorporation of CQDs in the TiO_2 photoanode [96]. It was also evident that CQDs improved the light absorption capacity of the TiO_2/CdS photoanode, which could lead to elevated electron-hole pair generation [24].

3.4. Photovoltaic performance of the QDSSCs

A schematic diagram for the photovoltaic devices investigated in this study is given in Fig. 8. Photoanodes were developed with two TiO_2 compact layers on top of FTO conducting glass substrates, followed by a CQD-incorporated mesoporous TiO_2 (TiO_2/CQD) layer. These photoanodes were sensitized with CdS QDs using the SILAR method. Upon light illumination, the electron-hole pair generation in CdS increases substantially. The excited electrons are injected into the conduction band (CB) of TiO_2, due to the favorable band alignment between the CBs of TiO_2 and CdS. These electrons are then transferred to the external circuit through the FTO layer and would ultimately reach the CE at the opposite end. Meanwhile, the electrolyte will provide electrons to the holes left in CdS QDs, regenerating them. The electrolyte species that get oxidized here are then transported towards the CE, where they are reduced back by accepting electrons from the CE. This process continues under light illumination, generating a continuous current flow through the circuit. However, some losses could be expected in these systems due to recombination reactions or back electron transfer processes at the interfaces [6,13,46]. The impact of CQD incorporation within the TiO_2 mesoporous layer for the performance of CdS QDDSCs will be discussed in detail in the subsequent sections.

In order to evaluate the photovoltaic performance of the modified photoanodes, the current density-voltage (*J-V*) characteristics of the CdS QDSSCs were assessed under simulated sunlight irradiation of 100 mW cm^{-2}. The power conversion efficiency (η) of photovoltaic devices is expressed as,

$$\eta = \frac{J_{SC} \times V_{OC} \times FF}{P_{in}} \times 100\% \quad (4)$$

where J_{SC} is the short circuit current density, V_{OC} is the open circuit voltage, and *FF* is the fill factor of the device [13,97]. During the study, the amount of CQDs incorporated in the photoanodes was varied to discover the optimum CQD amount associated with the best photovoltaic response. The calculated mean and standard error values of

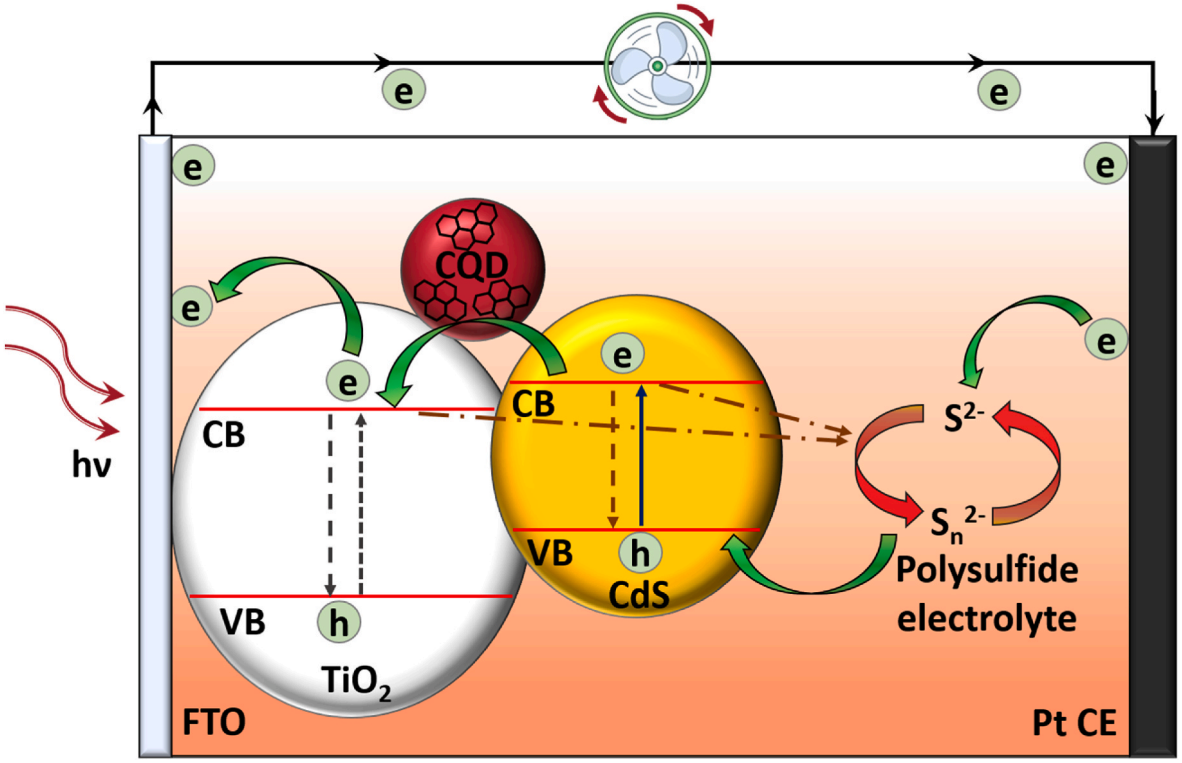

Fig. 8. Schematic diagram of the fabricated TiO_2/CQD/CdS/polysulfide electrolyte/Pt QDSSC.

Table 2
Photovoltaic parameters of QDSSCs assembled with TiO_2/CdS and TiO_2/CQD/CdS photoanodes.

Cells	CQD (μl) per 0.25 g of TiO_2 P25	V_{OC} (mV)	J_{SC} (mA cm^{-2})	*FF* (%)	Efficiency (%)
N	**0**	464 ± 3	7.78 ± 0.17	35.5 ± 0.7	1.28 ± 0.03
S1	**25**	468 ± 4	8.44 ± 0.18	35.8 ± 0.4	1.41 ± 0.02
S2	**50**	478 ± 2	9.24 ± 0.10	34.5 ± 0.5	1.52 ± 0.02
S3	**75**	481 ± 4	10.07 ± 0.14	34.8 ± 0.8	1.68 ± 0.03
S4	**100**	483 ± 4	9.81 ± 0.22	34.6 ± 0.6	1.64 ± 0.02

photovoltaic parameters acquired from multiple CdS QDSSCs with CQDs (S1-S4) and without CQDs (N) are tabulated in Table 2. When fabricating S1-S4 devices, the amount of CQDs was varied between 25 and 100 μl per 0.25g of TiO_2 in the TiO_2 P25 paste. It was observed that the V_{OC} of the devices kept increasing with the amount of CQDs, while the J_{SC} increased up to 75 μl of CQDs, and then started declining. Consequently, the best photovoltaic response was gained from the QDSSC prepared with 75 μl of CQDs (S3). When the performance of S3 devices was compared with the reference QDSSCs without CQDs (N), the *FF* was somewhat low; however, all the other parameters were improved. This was reflected in the current density-voltage (*J-V*) curves shown in Fig. 9 (a). The V_{OC} of the S3 devices was improved by 3.7 % from 464 mV (N) to 481 mV (S3), and the J_{SC} was notably increased by 29.4 % from 7.78 mA cm^{-2} (N) to 10.07 mA cm^{-2} (S3). Accordingly, the overall η of the S3 was improved by 31.3 % from 1.28 % (N) to 1.68 % (S3). Hence, the incorporation of CQDs in the TiO_2 photoanode could be suggested as an effective technique to enhance the photovoltaic performance of the CdS QDSSCs.

In order to understand the mechanism behind elevated photocurrent generation in the CQD incorporated devices, the incident photon conversion efficiency (IPCE) measurements were carried out. IPCE or the external quantum efficiency is a measure of photogenerated electrons per incident photons at a given wavelength [98,99]. The relationship between the photogenerated current density and IPCE can be expressed as,

$$IPCE\ (\%) = \frac{(1240 \times J_{SC})}{(\lambda \times I_i)} \times 100\% \quad (5)$$

where J_{SC} is the current density obtained by integrating the product of incident photon flux density, λ is the wavelength of the incident light, and I_i is the power of the incident light [97–100]. For the present study, IPCE data were recorded in the 300–650 nm wavelength range, as shown in Fig. 9 (b). A higher IPCE percentage was observed from the CdS QDSSC incorporated with CQDs, indicating better incident photon conversion rate [40,41]. This reaffirms the findings of the current density-voltage characterization, where a higher J_{SC} was reported with CQD incorporation. Most importantly, a negative shift was observed in the highest responsive wavelength region with the addition of CQDs. The IPCE of the CQD incorporated device peaked around 370 nm, while the IPCE of the device without CQDs peaked around 465 nm. This indicated an elevated conversion of higher energy photons to electrons in the CQD incorporated CdS QDSSCs. As the conditions for CdS QD sensitization remain the same for both devices, this was caused by the CQDs in the photoanode. CQDs act as energy down-conversion materials here, where they absorb higher energy photons and emit lower energy photons, which fall in the strong absorption region of CdS QDs [41, 101–103]. Hence, CQDs promote the photocurrent generation of CdS QDSSCs by effectively broadening the light absorption range towards the higher energy photons.

3.5. EIS characterization and Mott-Schottky analysis

Electrochemical impedance spectroscopic (EIS) measurements are frequently used in QDSSC studies to investigate interfacial charge transfer kinetics within these devices [46,104,105]. For the current study, EIS measurements of CdS QDSSCs, with and without CQDs, were taken under light illumination. The recorded EIS data were fitted with an equivalent electrical circuit model using the Zahner Analysis software. The resulting Nyquist plots and the equivalent electrical circuit model used for this study are shown in Fig. 10 (a), and the Bode phase plots are shown in Fig. 10 (b). In addition, the estimated EIS parameters are tabulated in Table 3. Two overlapped semicircles were observed in the obtained Nyquist plots, as shown in Fig. 10 (a). The first semicircle in the high-frequency region corresponds to the charge transfer kinetics at the CE/electrolyte interface, while the second semicircle in the mid-frequency region corresponds to the charge transfer kinetics at the photoanode/electrolyte interface. The elements in the equivalent circuit model represent the series resistance (R_S) of the device, the charge transfer resistance (R_{1CT}) and the chemical capacitance (CPE_1) at the CE/electrolyte interface, and the charge transfer resistance (R_{2CT}) and the chemical capacitance (CPE_2) at the photoanode/electrolyte interface [46,105]. According to the EIS parameters mentioned in Table 3, both R_S and R_{2CT} values improved in the case of the CQD incorporated device; however, a slight rise in the R_{1CT} value was also observed. Most importantly, a significant reduction of 32.7 Ω was observed in the R_{2CT}, the charge transfer resistance at the photoanode/electrolyte interface. This indicates more efficient charge transfer at the CQD incorporated

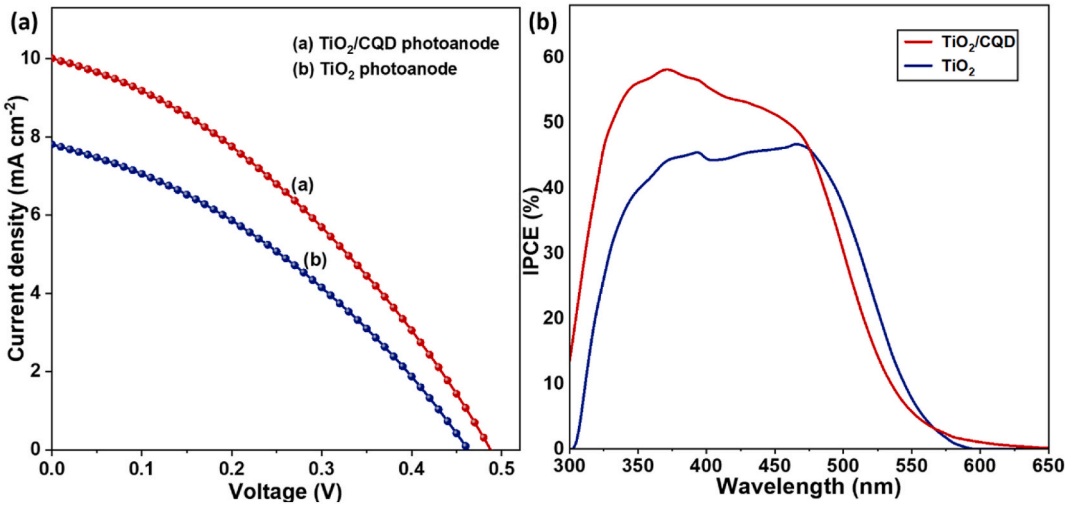

Fig. 9. (a) Current density-voltage (*J–V*) characteristics, and (b) IPCE spectra of QDSSCs assembled with TiO_2/CdS and TiO_2/CQD/CdS photoanodes.

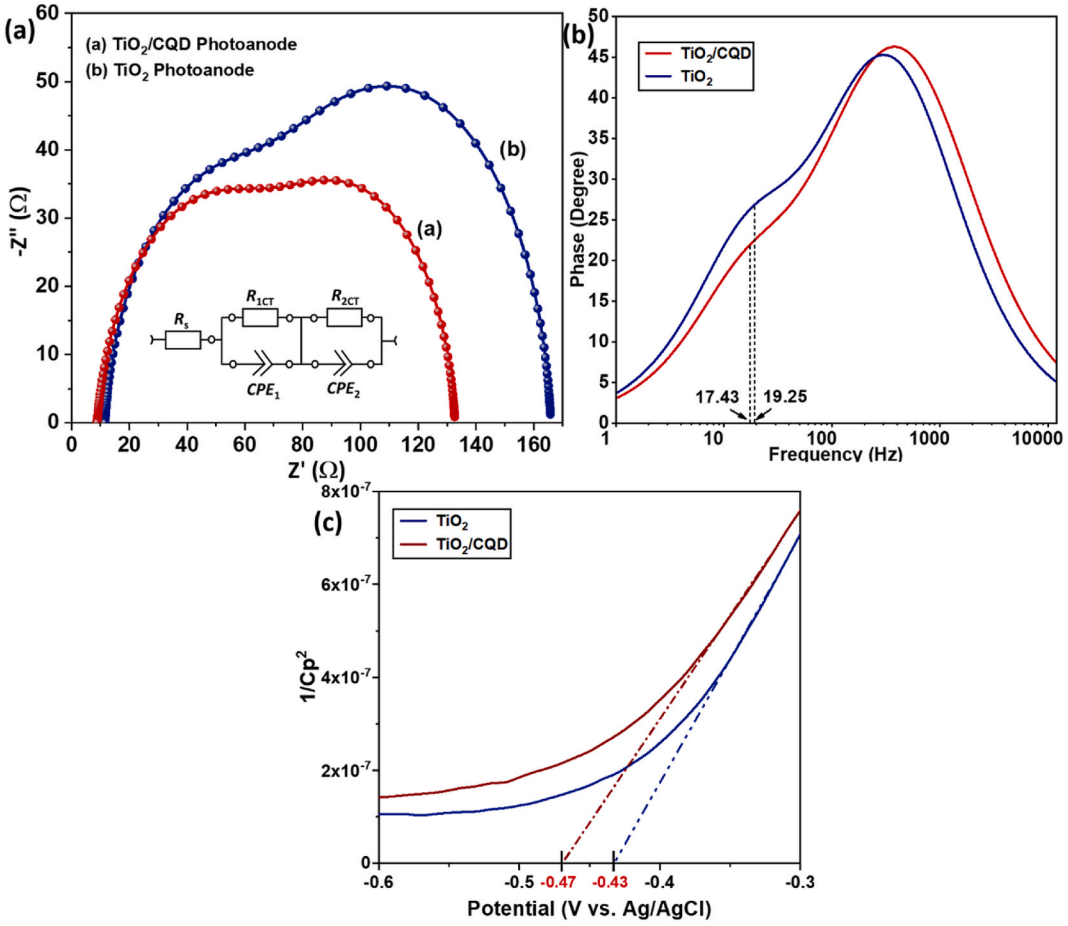

Fig. 10. EIS (a) Nyquist and (b) Bode phase plots of QDSSCs assembled with TiO_2/CdS and TiO_2/CQD/CdS photoanodes, and (c) Mott-Schottky plots of TiO_2 and TiO_2/CQD electrodes.

Table 3
EIS parameters of QDSSCs assembled with TiO_2 and TiO_2/CQD photoanodes under illuminated conditions.

Photoanode	R_s (Ω)	R_{1ct} (Ω)	R_{2ct} (Ω)	τ (ms)
TiO_2	11.60 Ω	61.5 Ω	92.8 Ω	8.3
TiO_2/CQD	8.84 Ω	63.8 Ω	60.1 Ω	9.1

photoanode/electrolyte interface, which could be due to higher photocurrent generation of the photoanode, as demonstrated in the previous current-voltage characterization and IPCE studies (Fig. 9) [40,105–107].

Additionally, the lifetime of the photo-generated electrons (τ) could be determined from the following relationship based on the frequency value of the peak appearing in the lower frequency region (f_{max}) of the Bode phase plots [30,105].

$$\tau = \frac{1}{2\pi f_{max}} \tag{6}$$

The τ shows an inverse relationship with the recombination at the photoanode/electrolyte interface [105]. Hence, the higher τ observed in the CQD incorporated device (9.1 ms), compared to the device without CQDs (8.3 ms), indicates a lower recombination rate at the photoanode/electrolyte interface [30,105,108]. Both R_{2CT} and τ values determined from the EIS analysis validate enhanced J_{SC} readings and the superior performance of the CQD incorporated photoanode.

The V_{OC} of QDSSCs is determined from the energy level difference between the quasi-Fermi level (E_f) of the photoanode and the redox potential of the electrolyte. Thus, a shift in the E_f in the negative direction will increase the energy level difference and consequently the V_{OC} of a device [109,110]. The flat band potential (V_{fb}) provides insight into the relative positioning of the Fermi levels, and could be determined from the x-axis intercepts of Mott-Schottky plots derived from the following equation,

$$\frac{1}{Cp^2} = \frac{2}{\varepsilon\varepsilon_0 A^2 e N_D}\left(V - V_{fb} - \frac{k_B T}{e}\right) \tag{7}$$

where Cp is the solid/liquid interfacial capacitance, ε is the dielectric constant of the semiconductor, ε_0 is the permittivity of the free space, A is the area, e is the electronic charge, N_D is the donor density, V is the applied potential, k_B is Boltzmann's constant, and T is the absolute temperature [104,110–112]. The V_{fb} values calculated from the Mott-Schottky plots (Fig. 10 (c)) were −0.40 and −0.44 V for the TiO_2 and TiO_2/CQD electrodes. This negative shift in the V_{fb} due to the incorporation of CQDs in the TiO_2 electrode indicates an upward shift in E_f, which correlates with the higher V_{OC} values reported in the previous current-density voltage studies [104,109,110].The shift in E_f, could be due to energy states originating in TiO_2 due to attached CQDs. The upward shift in the Fermi level promotes charge separation and transport in the photoanode [113].

4. Conclusion

In this study, carbon quantum dots were successfully incorporated into the TiO_2/CdS photoanodes to enhance the photovoltaic performance of QDSSCs. CQDs, with an average diameter of ~3 nm, were

synthesized following a cold atmospheric plasma method. CQD incorporation in the photoanode was achieved by mixing CQD solution in the TiO_2 doctor blade paste. The incorporation of CQDs in the photoanodes enhanced the overall power conversion efficiency of CdS QDSSCs from 1.28 % to 1.68 %, with an overall increase of 31.3 %. The charge transfer resistance at the photoanode/electrolyte interface was reduced significantly by 54.4 % with the incorporation of CQD, due to efficient photocurrent generation and the low recombination in the photoanode. Thus, incorporation of CQDs in the photoanodes could be considered an effective technique for enhancing the photovoltaic performance of QDSSCs.

CRediT authorship contribution statement

W.I. Sandamali: Writing – original draft, Methodology, Investigation, Formal analysis, Data curation. **G.K.R. Senadeera:** Writing – review & editing, Supervision, Resources, Project administration, Methodology, Funding acquisition, Conceptualization. **Janith Weerasinghe:** Writing – review & editing, Resources, Investigation. **V.P.S. Perera:** Supervision, Funding acquisition. **M.A.K.L. Dissanayake:** Supervision, Resources, Project administration, Methodology, Funding acquisition, Conceptualization.

Statement of novelty

The work described in this article is original and has not been published previously. This work has not been submitted previously in part or in whole, and it is not under consideration for publication elsewhere.

Declaration of competing interest

The authors declare that they have no known competing financial interests or personal relationships that could have appeared to influence the work reported in this paper.

Acknowledgement

This research was financially supported by the research grant (DOR9 2019) awarded by the Accelerating Higher Education Expansion and Development (AHEAD) Operation of the Ministry of Higher Education in Sri Lanka, funded by the World Bank.

Data availability

Data will be made available on request.

References

[1] J. Pastuszak, P. Węgierek, Photovoltaic cell generations and current research directions for their development, Materials 15 (2022), https://doi.org/10.3390/ma15165542.
[2] G.P. Darshan, D.R. Lavanya, B. Daruka Prasad, S.C. Sharma, H. Nagabhushana, Quantum Dots-based Solar Cells: Futuristic Green Technology to Accomplish the Energy Crisis, Elsevier Ltd, 2023.
[3] L.C. Hirst, 1.12 - principles of solar energy conversion, Compr Renew Energy (2022) 234–255, https://doi.org/10.1016/B978-0-12-819727-1.00112-6. Second Ed Vol 1-9 1.
[4] A. Kausar, Chapter 1 - quantum dots: an introduction to the basics and classification, in: A. Kausar (Ed.), Graphene Quantum Dots and their Derived Nanocomposites, Elsevier, 2025, pp. 1–21.
[5] S. Kumar, N. Patra, I. Hossain, A. Thakur, T. Jaseetharan, N.G. Shimpi, Exponential developments of quantum dots ecosystem for solar energy conversion and photocatalytic reactions: from photoanode design to renewable energy applications, Mater. Res. Bull. 184 (2025) 113223, https://doi.org/10.1016/j.materresbull.2024.113223.
[6] G. Shilpa, P.M. Kumar, D.K. Kumar, P.R. Deepthi, V. Sadhu, A. Sukhdev, R. R. Kakarla, Recent advances in the development of high efficiency quantum dot sensitized solar cells (QDSSCs): a review, Mater. Sci. Energy Technol. 6 (2023) 533–546, https://doi.org/10.1016/j.mset.2023.05.001.
[7] NREL, Best research-cell efficiency chart. https://www2.nrel.gov/pv/cell-efficiency, 2025. (Accessed 12 May 2025).
[8] W. Shockley, H.J. Queisser, Detailed balance limit of efficiency of p-n junction solar cells, J. Appl. Phys. 32 (1961) 510–519, https://doi.org/10.1063/1.1736034.
[9] Y. Xu, T. Gong, J.N. Munday, The generalized shockley-Queisser limit for nanostructured solar cells, Sci. Rep. 5 (2015) 1–9, https://doi.org/10.1038/srep13536.
[10] N. Thi, K. Chung, P.T. Nguyen, H.T. Tung, D.H. Phuc, Quantum dot sensitized solar cell : photoanodes , counter, Molecules 26 (2021) 1–21.
[11] B.B. Kasaye, M.W. Shura, S.T. Dibaba, Review of recent progress in the development of electrolytes for Cd/Pb-based quantum dot-sensitized solar cells: performance and stability, RSC Adv. 14 (2024) 16255–16268, https://doi.org/10.1039/d4ra01030b.
[12] H.K. Jun, H.T. Tung, A short overview on recent progress in semiconductor quantum dot-sensitized solar cells, J. Nanomater. (2022), https://doi.org/10.1155/2022/1382580, 2022.
[13] M.A. Basit, M. Aanish Ali, Z. Masroor, Z. Tariq, J.H. Bang, Quantum dot-sensitized solar cells: a review on interfacial engineering strategies for boosting efficiency, J. Ind. Eng. Chem. 120 (2023) 1–26, https://doi.org/10.1016/j.jiec.2022.12.016.
[14] P.V. Tumram, R. Nafdey, P.R. Kautkar, S.V. Agnihotri, R.A. Khaparde, S. P. Wankhede, S.V. Moharil, Solar cell performance enhancement using nanostructures, Mater. Sci. Eng. B 307 (2024) 117504, https://doi.org/10.1016/j.mseb.2024.117504.
[15] S. Sikiru, T.L. Oladosu, S.Y. Kolawole, L.A. Mubarak, H. Soleimani, L.O. Afolabi, A.O. Oluwafunke Toyin, Advance and prospect of carbon quantum dots synthesis for energy conversion and storage application: a comprehensive review, J. Energy Storage 60 (2023) 106556, https://doi.org/10.1016/j.est.2022.106556.
[16] M. Roostaee, R. Ranjbar-Karimi, Emerging trends in carbon quantum dots: synthesis, characterization, and environmental photodegradation applications, Mater. Sci. Semicond. Process. 188 (2025) 109212, https://doi.org/10.1016/j.mssp.2024.109212.
[17] Y. Wang, A. Hu, Carbon quantum dots: synthesis, properties and applications, J. Mater. Chem. C 2 (2014) 6921–6939, https://doi.org/10.1039/c4tc00988f.
[18] X. Xu, R. Ray, Y. Gu, H.J. Ploehn, L. Gearheart, K. Raker, W.A. Scrivens, Electrophoretic analysis and purification of fluorescent single-walled carbon nanotube fragments, J. Am. Chem. Soc. 126 (2004) 12736–12737, https://doi.org/10.1021/ja040082h.
[19] Ahmed HE. Hassan, M. Soylak, Exploring the potential of carbon quantum dots (CQDs) as an advanced nanomaterial for effective sensing and extraction of toxic pollutants, TrAC, Trends Anal. Chem. 180 (2024) 117939, https://doi.org/10.1016/j.trac.2024.117939.
[20] B. Acharya, A. Behera, S. Behera, S. Moharana, Carbon quantum dots: a systematic overview of recent developments in synthesis, properties, and novel therapeutic applications, Inorg. Chem. Commun. 165 (2024) 112492, https://doi.org/10.1016/j.inoche.2024.112492.
[21] A. Ben Amor, H. Hemmami, I. Ben Amor, S. Zeghoud, A. Alnazza Alhamad, M. Belkacem, N.S. Nair, A.B. Sruthimol, Advances in carbon quantum dot applications:Catalysis, sensing, and biomedical innovations, Mater. Sci. Semicond. Process. 185 (2025) 108945, https://doi.org/10.1016/j.mssp.2024.108945.
[22] O.K. Mmelesi, L.L. Mguni, F tang Li, B. Nkosi, X. Liu, Recent development in fluorescent carbon quantum dots-based photocatalysts for water and energy applications, Mater. Sci. Semicond. Process. 181 (2024) 108661, https://doi.org/10.1016/j.mssp.2024.108661.
[23] V. Arias Velasco, A.C. Agudelo, D. Hotza, S.Y. Gómez González, Context and prospects of carbon quantum dots applied to environmental solutions, Environ. Nanotechnol. Monit. Manag. 20 (2023), https://doi.org/10.1016/j.enmm.2023.100884.
[24] P. Kumar, S. Dua, R. Kaur, M. Kumar, G. Bhatt, A review on advancements in carbon quantum dots and their application in photovoltaics, RSC Adv. 12 (2022) 4714–4759, https://doi.org/10.1039/d1ra08452f.
[25] V. Magesh, A.K. Sundramoorthy, D. Ganapathy, Recent advances on synthesis and potential applications of carbon quantum dots, Front. Mater. 9 (2022) 1–27, https://doi.org/10.3389/fmats.2022.906838.
[26] S. Riaz, S.J. Park, Thioacetamide-derived nitrogen and sulfur co-doped carbon quantum dots for “green” quantum dot solar cells, J. Ind. Eng. Chem. 105 (2022) 111–120, https://doi.org/10.1016/j.jiec.2021.09.009.
[27] P.M. Olmos-Moya, S. Velazquez-Martinez, C. Pineda-Arellano, J.R. Rangel-Mendez, L.F. Chazaro-Ruiz, High added value functionalized carbon quantum dots synthetized from orange peels by assisted microwave solvothermal method and their performance as photosensitizer of mesoporous TiO2 photoelectrodes, Carbon N Y 187 (2022) 216–229, https://doi.org/10.1016/j.carbon.2021.11.003.
[28] S. Riaz, S.J. Park, Carbon quantum dots-embedded graphitic carbon nitride nanotubes for enhancing the power conversion efficiency of sensitized solar cells, Mater. Today Chem. 24 (2022) 100763, https://doi.org/10.1016/j.mtchem.2021.100763.
[29] R. Paneru, X. Kang, S. Budhathoki, Z. Chen, Q. Yang, S.T. Tjeng, Q. Dai, W. Wang, J. Tang, M. Fan, Enhancement effect of biomass-derived carbon quantum dots (Cqds) on the performance of dye-sensitized solar cells (Dsscs), Available SSRN 4849238 1–13, https://doi.org/10.1016/j.jes.2024.10.001, 2024.
[30] R. Cheruku, J.H. Kim, V.B.M. Krishna, P. Periyat, S.D. Sssr, Photo-electrodes decorated with carbon quantum dots: efficient dye-sensitized solar cells, Results Eng. 20 (2023) 101611, https://doi.org/10.1016/j.rineng.2023.101611.
[31] S. Jahanbani, R. Ghadari, Investigating the effect of nitrogen and chlorine Co–doped carbon quantum dots in phenazine and quinoxaline sensitized solar

cells, Electrochim. Acta 497 (2024) 144580, https://doi.org/10.1016/j.electacta.2024.144580.
[32] Kurukavak Ç. Kırbıyık, A. Büyükbekar, M. Tok, T. Yılmaz, M. Kuş, M. Ersöz, Modification and performance enhancement of P3HT:PCBM based organic solar cells incorporated with phosphorus doped carbon quantum dots, Chem. Phys. Lett. 845 (2024), https://doi.org/10.1016/j.cplett.2024.141300.
[33] D.C.T. Nguyen, B.S. Kim, G.H. Oh, V.P. Vu, S. Kim, S.H. Lee, Incorporation of carbon quantum dots with PEDOT:PSS for high-performance inverted organic solar cells, Synth. Met. 298 (2023) 117430, https://doi.org/10.1016/j.synthmet.2023.117430.
[34] Z. Wang, B. He, M. Wei, W. Liu, X. Li, J. Zhu, H. Chen, Q. Tang, Enhanced charge extraction enabled by amide-functionalized carbon quantum dots modifier for efficient carbon-based perovskite solar cells, Chem. Eng. J. 479 (2024) 147736, https://doi.org/10.1016/j.cej.2023.147736.
[35] Y. Kumar, L. Yadav, A. Singh, R.K. Gupta, K.S. Nalwa, A. Garg, Waste-derived carbon quantum dots for improving the photostability of perovskite solar cells to > 1,000 h, Mater. Today Energy 44 (2024) 101654, https://doi.org/10.1016/j.mtener.2024.101654.
[36] Y.C. Yen, P.H. Hsiao, S.H. Chen, C.Y. Chen, Incorporation of carbon quantum-dot films with silicon substrates for improved photovoltaic performances, Mater. Lett. 364 (2024) 136359, https://doi.org/10.1016/j.matlet.2024.136359.
[37] P. Kumar, A. Mahapatra, S. Kumar, B. Pradhan, Photovoltaic Application of Carbon Quantum Dots, LTD, 2023.
[38] X. Guo, H. Zhang, H. Sun, M.O. Tade, S. Wang, Green synthesis of carbon quantum dots for sensitized solar cells, ChemPhotoChem 1 (2017) 116–119, https://doi.org/10.1002/cptc.201600038.
[39] P. Huang, S. Xu, M. Zhang, W. Zhong, Z. Xiao, Y. Luo, Green allium fistulosum derived nitrogen self-doped carbon dots for quantum dot-sensitized solar cells, Mater. Chem. Phys. 240 (2020) 122158, https://doi.org/10.1016/j.matchemphys.2019.122158.
[40] P. Huang, S. Xu, M. Zhang, W. Zhong, Z. Xiao, Y. Luo, Carbon quantum dots improving photovoltaic performance of CdS quantum dot-sensitized solar cells, Opt. Mater. 110 (2020) 110535, https://doi.org/10.1016/j.optmat.2020.110535.
[41] C. Zhao, X. Zhang, X. Shu, X. Liu, D. Fang, Y. Song, J. Wang, Er-doped carbon dots broadening light absorption range and accelerating electron transport for enhancing photovoltaic performance of CdS quantum dots sensitized cells, Opt. Mater. 84 (2018) 242–251, https://doi.org/10.1016/j.optmat.2018.07.016.
[42] J. Weerasinghe, J. Scott, A.D.K. Deshan, D. Chen, A. Singh, S. Sen, P. Sonar, K. Vasilev, Q. Li, K. Ostrikov, Monochromatic blue and switchable blue-green carbon quantum dots by room-temperature air plasma processing, Adv. Mater. Technol. 7 (2022) 1–9, https://doi.org/10.1002/admt.202100586.
[43] B.H. Adil, A.S. Obaid, M.M.F. Al-Halbosiy, H.H. Murbat, Use of cold plasma in the synthesis of gold nanomaterials for parasitic leishmaniasis treatment, Int J Plasma Environ Sci Technol 14 (2020) 1–7, https://doi.org/10.34343/ijpest.2020.14.e02005.
[44] M. Velusamy, M. Radhakrishnan, Chemistry of cold plasma technology, Chem Therm Non-Thermal Food Process Technol (2024) 235–257, https://doi.org/10.1016/B978-0-443-22182-8.00012-7.
[45] F.M. De Souza, R.K. Gupta, G. Yasin, T.A. Nguyen, Plasma Technology for Nanostructures, Elsevier Inc, 2022.
[46] G.K.R. Senadeera, W.I. Sandamali, J.M.K.W. Kumari, T. Jaseetharan, J. Weerasinghe, P. Sonar, V.P.S. Perera, J.C.N. Rajendra, N. Karthikeyan, M.A.K. L. Dissanayake, Morphological and structural study on low cost SnO2 counter electrode and its applications in quantum dot sensitized solar cells with polysulfide electrolyte, Mater Sci Eng B Solid-State Mater Adv Technol 286 (2022) 116075, https://doi.org/10.1016/j.mseb.2022.116075.
[47] S.W. Chong, C.W. Lai, J.C. Juan, B.F. Leo, An investigation on surface modified TiO2 incorporated with graphene oxide for dye-sensitized solar cell, Sol. Energy 191 (2019) 663–671, https://doi.org/10.1016/j.solener.2019.08.065.
[48] N.D. Johari, Z.M. Rosli, J.M. Juoi, S.A. Yazid, Comparison on the TiO2 crystalline phases deposited via dip and spin coating using green sol-gel route, J. Mater. Res. Technol. 8 (2019) 2350–2358, https://doi.org/10.1016/j.jmrt.2019.04.018.
[49] J. Zemann, Crystal structures,2nd Edition. Vol. 1by R. W. G. Wyckoff, 1965.
[50] M. Rahbar, M. Mehrzad, M. Behpour, S. Mohammadi-Aghdam, M. Ashrafi, S, N co-doped carbon quantum dots/TiO2 nanocomposite as highly efficient visible light photocatalyst, Nanotechnology 30 (2019), https://doi.org/10.1088/1361-6528/ab40dc.
[51] M. Samir, Z. Ismail, A.M. Agour, H. Nageh, S.O. Abdellatif, Exploring forward scattering mechanisms in TiO2 with carbon quantum dots: insights into photovoltaic applications, Opt. Mater. 148 (2024) 114922, https://doi.org/10.1016/j.optmat.2024.114922.
[52] M. Shafique, M.S. Mahr, M. Yaseen, H.N. Bhatti, CQD/TiO2 nanocomposite photocatalyst for efficient visible light-driven purification of wastewater containing methyl orange dye, Mater. Chem. Phys. 278 (2022) 125583, https://doi.org/10.1016/j.matchemphys.2021.125583.
[53] M. Sahadat Hossain, S. Ahmed, Easy and green synthesis of TiO2 (Anatase and Rutile): estimation of crystallite size using Scherrer equation, Williamson-Hall plot, Monshi-Scherrer Model, size-strain plot, Halder- Wagner Model, Results Mater. 20 (2023) 100492, https://doi.org/10.1016/j.rinma.2023.100492.
[54] B. Lafuente, R.T. Downs, H. Yang, N. Stone, The Power of Databases: the RRUFF Project, 2016.
[55] R.A. Spurr, H. Myers, Quantitative Analysis of Anatase-Rutile Mixtures with an X-Ray Diffractometer, 1957.
[56] W.H. Bragg, W.L. Bragg, The reflection of X-rays by crystals, Proc. R. Soc. Lond. - Ser. A Contain. Pap. a Math. Phys. Character 88 (1913) 428–438, https://doi.org/10.1098/rspa.1913.0040.
[57] O.A. Voronov, K.W. Street, Raman scattering in a new carbon material, Diam. Relat. Mater. 19 (2010) 31–39, https://doi.org/10.1016/j.diamond.2009.10.018.
[58] I. Childres, L. Jauregui, W. Park, H. Caoa, Y.P. Chena, Raman spectroscopy of graphene and related materials, New Dev Phot Mater Res (2013) 403–418.
[59] J. George, S. Upadhyay, M. Balachandran, Exploration of graphene layers in various carbon materials by raman spectroscopic techniques, Mapana J Sci 20 (2021) 65–81, https://doi.org/10.12723/mjs.59.5.
[60] A.C. Ferrari, J. Robertson, Interpretation of Raman spectra of disordered and amorphous carbon, Phys. Rev. B 61 (2000) 14095–14107, https://doi.org/10.1103/PhysRevB.61.14095.
[61] C.C. Zhang, S. Hartlaub, I. Petrovic, B. Yilmaz, Raman spectroscopy characterization of amorphous coke generated in industrial processes, ACS Omega 7 (2022) 2565–2570, https://doi.org/10.1021/acsomega.1c03456.
[62] S. Botti, A. Rufoloni, T. Rindzevicius, M.S. Schmidt, Surface-enhanced raman spectroscopy characterization of pristine and functionalized carbon nanotubes and graphene, Raman Spectrosc (2018), https://doi.org/10.5772/intechopen.74065.
[63] P.R. Varadwaj, V.A. Dinh, Y. Morikawa, R. Asahi, Polymorphs of titanium dioxide: an assessment of the variants of projector augmented wave potential of titanium on their geometric and dielectric properties, ACS Omega 8 (2023) 22003–22017, https://doi.org/10.1021/acsomega.3c02038.
[64] A.M. Borisov, A.V. Makunin, E.S. Mashkova, V.A. Kazakov, M.A. Ovchinnikov, V. V. Sleptsov, Ion-beam modification of carbon textile Busofit T-040, J Phys Conf Ser 1121 (2018), https://doi.org/10.1088/1742-6596/1121/1/012008.
[65] Y. Yin, J. Yin, W. Zhang, H. Tian, Z. Hu, M. Ruan, Z. Song, L. Liu, Effect of char structure evolution during pyrolysis on combustion characteristics and kinetics of waste biomass, J Energy Resour Technol Trans ASME 140 (2018), https://doi.org/10.1115/1.4039445.
[66] G. Rajender, P.K. Giri, Formation mechanism of graphene quantum dots and their edge state conversion probed by photoluminescence and Raman spectroscopy, J. Mater. Chem. C 4 (2016) 10852–10865, https://doi.org/10.1039/c6tc03469a.
[67] A. Sacco, L. Mandrile, L.L. Tay, N. Itoh, A. Raj, A. Moure, A. Del Campo, J. F. Fernandez, K.R. Paton, S. Wood, H. Kwon, T. Adel, A.R. Hight Walker, E. H. Martins Ferreira, R. Theissmann, T. Koch, A.M. Giovannozzi, C. Portesi, A. M. Rossi, Quantification of titanium dioxide (TiO2) anatase and rutile polymorphs in binary mixtures by Raman spectroscopy: an interlaboratory comparison, Metrologia 60 (2023), https://doi.org/10.1088/1681-7575/acf76d.
[68] D. Liu, X. Chen, Y. Hu, T. Sun, Z. Song, Y. Zheng, Y. Cao, Z. Cai, M. Cao, L. Peng, Y. Huang, L. Du, W. Yang, G. Chen, D. Wei, A.T.S. Wee, D. Wei, Raman enhancement on ultra-clean graphene quantum dots produced by quasi-equilibrium plasma-enhanced chemical vapor deposition, Nat. Commun. 9 (2018) 1–10, https://doi.org/10.1038/s41467-017-02627-5.
[69] H. Lai, F. Xu, Y. Zhang, L. Wang, Recent progress on graphene-based substrates for surface-enhanced Raman scattering applications, J. Mater. Chem. B 6 (2018) 4008–4028, https://doi.org/10.1039/c8tb00902c.
[70] X. Liang, N. Li, R. Zhang, P. Yin, C. Zhang, N. Yang, K. Liang, B. Kong, Carbon-based SERS biosensor: from substrate design to sensing and bioapplication, NPG Asia Mater. 13 (2021), https://doi.org/10.1038/s41427-020-00278-5.
[71] A. Reddy, F. Islam, P.K. Singh, M. Diantoro, Enhancing the properties of PEG-based solid polymer electrolytes with TiO 2 nanoparticles for potassium ion batteries, Chem. Phys. Impact 10 (2025) 100788, https://doi.org/10.1016/j.chphi.2024.100788.
[72] F.X. Nobre, F.A.F. Mariano, F.E.P. Santos, M.L.M. Rocco, L. Manzato, J.M.E. De Matos, P.R.C. Couceiro, W.R. Brito, Heterogeneous photocatalysis of Tordon 2,4-D herbicide using the phase mixture of TiO2, J. Environ. Chem. Eng. 7 (2019) 103501, https://doi.org/10.1016/j.jece.2019.103501.
[73] NIST X-ray photoelectron spectroscopy database, NIST Standard Reference Database Number 20, National Institute of Standards and Technology, Gaithersburg MD, 20899, 2000. https://srdata.nist.gov/xps/. (Accessed 2 May 2025).
[74] J. Peng, X. Kang, S. Zhao, Y. Yin, P. Zhao, A.J. Ragauskas, C. Si, X. Song, Regulating the properties of activated carbon for supercapacitors: impact of particle size and degree of aromatization of hydrochar, Adv. Compos. Hybrid Mater. 6 (2023) 1–39, https://doi.org/10.1007/s42114-023-00682-9.
[75] S. Tong, J. Zhou, L. Ding, C. Zhou, Y. Liu, S. Li, J. Meng, S. Zhu, S. Chatterjee, F. Liang, Preparation of carbon quantum dots/TiO2 composite and application for enhanced photodegradation of rhodamine B, Colloids Surfaces A Physicochem Eng Asp 648 (2022) 129342, https://doi.org/10.1016/j.colsurfa.2022.129342.
[76] A. Rezaei, L. Hadian-Dehkordi, H. Samadian, M. Jaymand, H. Targhan, A. Ramazani, H. Adibi, X. Deng, L. Zheng, H. Zheng, Pseudohomogeneous metallic catalyst based on tungstate-decorated amphiphilic carbon quantum dots for selective oxidative scission of alkenes to aldehyde, Sci. Rep. 11 (2021) 1–14, https://doi.org/10.1038/s41598-021-83863-0.
[77] L. Tang, R. Ji, X. Cao, J. Lin, H. Jiang, X. Li, K.S. Teng, C.M. Luk, S. Zeng, J. Hao, S.P. Lau, Deep ultraviolet photoluminescence of water-soluble self-passivated graphene quantum dots, ACS Nano 6 (2012) 5102–5110, https://doi.org/10.1021/nn300760g.
[78] Y. Xu, S. Wu, P. Wan, J. Sun, Z.D. Hood, Introducing Ti3+ defects based on lattice distortion for enhanced visible light photoreactivity in TiO2 microspheres, RSC Adv. 7 (2017) 32461–32467, https://doi.org/10.1039/c7ra04885h.
[79] B. Bharti, S. Kumar, H.N. Lee, R. Kumar, Formation of oxygen vacancies and Ti3+ state in TiO2 thin film and enhanced optical properties by air plasma treatment, Sci. Rep. 6 (2016) 1–12, https://doi.org/10.1038/srep32355.
[80] S.E. Glassford, B. Byrne, S.G. Kazarian, Recent applications of ATR FTIR spectroscopy and imaging to proteins, Biochim. Biophys. Acta, Proteins

Proteomics 1834 (2013) 2849–2858, https://doi.org/10.1016/j.bbapap.2013.07.015.
[81] S.G. Kazarian, K.L.A. Chan, ATR-FTIR spectroscopic imaging: recent advances and applications to biological systems, Analyst 138 (2013) 1940–1951, https://doi.org/10.1039/c3an36865c.
[82] R.A. Arias-Niquepa, J.J. Prías-Barragán, H. Ariza-Calderón, M.E. Rodríguez-García, Activated carbon obtained from bamboo: synthesis, morphological, vibrational, and electrical properties and possible temperature sensor, Phys Status Solidi Appl Mater Sci 216 (2019) 1–11, https://doi.org/10.1002/pssa.201800422.
[83] K. Surana, R.M. Mehra, S.S. Soni, B. Bhattacharya, Real-time photovoltaic parameters assessment of carbon quantum dots showing strong blue emission, RSC Adv. 12 (2022) 1352–1360, https://doi.org/10.1039/d1ra07634e.
[84] J. Zhuang, M. Li, Y. Pu, A.J. Ragauskas, C.G. Yoo, Observation of potential contaminants in processed biomass using fourier transform infrared spectroscopy, Appl. Sci. 10 (2020) 1–13, https://doi.org/10.3390/app10124345.
[85] O.J. Gbadeyan, L.Z. Linganiso, N. Deenadayalu, Assessment and optimization of thermal stability and water absorption of loading snail shell nanoparticles and sugarcane bagasse cellulose fibers on polylactic acid bioplastic films, Polymers 15 (2023), https://doi.org/10.3390/polym15061557.
[86] M. Manfredi, E. Barberis, A. Rava, E. Robotti, F. Gosetti, E. Marengo, Portable diffuse reflectance infrared fourier transform (DRIFT) technique for the non-invasive identification of canvas ground: IR spectra reference collection, Anal. Methods 7 (2015) 2313–2322, https://doi.org/10.1039/c4ay02006e.
[87] A. Abbas, T.A. Tabish, S.J. Bull, T.M. Lim, A.N. Phan, High yield synthesis of graphene quantum dots from biomass waste as a highly selective probe for Fe3+ sensing, Sci. Rep. 10 (2020) 1–16, https://doi.org/10.1038/s41598-020-78070-2.
[88] Ö.K. Koç, A. Üzer, R. Apak, Heteroatom-doped carbon quantum dots and polymer composite as dual-mode nanoprobe for fluorometric and colorimetric determination of picric acid, ACS Appl. Mater. Interfaces 15 (2023) 42066–42079, https://doi.org/10.1021/acsami.3c07938.
[89] T. Schmitt, F. Rosi, E. Mosconi, K. Shull, S. Fantacci, C. Miliani, K. Gray, New insights into the deterioration of TiO2 based oil paints: the effects of illumination conditions and surface interactions, Herit Sci 10 (2022) 1–16, https://doi.org/10.1186/s40494-022-00733-2.
[90] C. Afonso, I.R. Segundo, O. Lima, S. Landi, N. Homem, M.F.M. Costa, E. Freitas, J. Carneiro, Optical, structural, morphological and chemical properties of doped TiO2nanoparticles with FeCl3, J Phys Conf Ser 2407 (2022), https://doi.org/10.1088/1742-6596/2407/1/012001.
[91] S. Briche, M. Derqaoui, M. Belaiche, E.M. El Mouchtari, P. Wong-Wah-Chung, S. Rafqah, Nanocomposite material from TiO2 and activated carbon for the removal of pharmaceutical product sulfamethazine by combined adsorption/photocatalysis in aqueous media, Environ. Sci. Pollut. Res. 27 (2020) 25523–25534, https://doi.org/10.1007/s11356-020-08939-2.
[92] T. Dutta, O. Chatterjee, B. Chakraborty, A.L. Koner, Photophysical Properties of Carbon Quantum Dots, LTD, 2023.
[93] T. Paul, M.R. Jose, K.A.A. Mary, Multicolor emissive carbon quantum dots/Tb3+@SiO2 for solid lighting applications, Opt. Commun. 577 (2025) 131444, https://doi.org/10.1016/j.optcom.2024.131444.
[94] S. Sharma, P. Chowdhury, Tunable dual photoluminescence from synthesized urea-based carbon quantum dots: a DFT based simulation on structural insights, Opt. Mater. 153 (2024) 115617, https://doi.org/10.1016/j.optmat.2024.115617.
[95] I. Diwan, G. Kant, P. Swarup, Synthesis of green fluorescent , energy efficient nitrogen doped carbon quantum dots, Optik 303 (2024) 171725, https://doi.org/10.1016/j.ijleo.2024.171725.
[96] H. Luo, S. Dimitrov, M. Daboczi, J. Kim, Q. Guo, Y. Fang, M.A. Stoeckel, P. Samori, O. Fenwick, B.J. Sobrido, X. Wang, M. Titirici, Nitrogen-Doped Carbon Dots/TiO2 Nanoparticle Composites for Photoelectrochemical Water Oxidation, ACS Appl. Nano Mater. 3 (2020) 3371–3381. https://doi.org/10.1021/acsanm.9b02412.
[97] M. Kouhnavard, S. Ikeda, N.A. Ludin, N.B. Ahmad Khairudin, B.V. Ghaffari, M. A. Mat-Teridi, M.A. Ibrahim, S. Sepeai, K. Sopian, A review of semiconductor materials as sensitizers for quantum dot-sensitized solar cells, Renew. Sustain. Energy Rev. 37 (2014) 397–407, https://doi.org/10.1016/j.rser.2014.05.023.
[98] D.S. Ellis, Y. Piekner, D.A. Grave, P. Schnell, A. Rothschild, Considerations for the accurate measurement of incident photon to current efficiency in photoelectrochemical cells, Front. Energy Res. 9 (2022) 1–14, https://doi.org/10.3389/fenrg.2021.726069.
[99] C. Li, H. Wu, L. Zhu, J. Xiao, Y. Luo, D. Li, Q. Meng, C. Li, H. Wu, L. Zhu, J. Xiao, Y. Luo, D. Li, Study on negative incident photon-to-electron conversion efficiency of quantum dot- sensitized solar cells study on negative incident photon-to-electron conversion efficiency of quantum dot-sensitized solar cells, Rev. Sci. Instrum. 85 (2014) 023103, https://doi.org/10.1063/1.4865115.
[100] X.Z. Guo, Y.H. Luo, C.H. Li, D. Qin, D.M. Li, Q.B. Meng, Can the incident photo-to-electron conversion efficiency be used to calculate short-circuit current density of dye-sensitized solar cells, Curr. Appl. Phys. 12 (2012) e54–e58, https://doi.org/10.1016/j.cap.2011.03.060.
[101] R. Datt, S. Bishnoi, D. Hughes, P. Mahajan, A. Singh, R. Gupta, S. Arya, V. Gupta, W.C. Tsoi, Downconversion materials for perovskite solar cells, Sol. RRL 6 (2022), https://doi.org/10.1002/solr.202200266.
[102] A.S. Rasal, S. Yadav, A. Yadav, A.A. Kashale, S.T. Manjunatha, A. Altaee, J. Y. Chang, Carbon quantum dots for energy applications: a review, ACS Appl. Nano Mater. 4 (2021) 6515–6541, https://doi.org/10.1021/acsanm.1c01372.
[103] J. Kong, Y. Wei, F. Zhou, L. Shi, S. Zhao, M. Wan, X. Zhang, Carbon Quantum Dots: Properties, Preparation, and Applications, 2024.
[104] I.R. Jo, Y.H. Lee, H. Kim, K.S. Ahn, Multifunctional nitrogen-doped graphene quantum dots incorporated into mesoporous TiO2 films for quantum dot-sensitized solar cells, J. Alloys Compd. 870 (2021) 159527, https://doi.org/10.1016/j.jallcom.2021.159527.
[105] M.A.K.L. Dissanayake, T. Jaseetharan, G.K.R. Senadeera, C.A. Thotawatthage, A novel, pbs:hg quantum dot-sensitized, highly efficient solar cell structure with triple layered TiO2 photoanode, Electrochim. Acta 269 (2018) 172–179, https://doi.org/10.1016/j.electacta.2018.02.140.
[106] S. Mahalingam, R. Rabeya, A. Manap, K.S. Lau, C.H. Chia, N. Afandi, A. Omar, Electron transport in heteroatom-doped graphene quantum dots for TiO2-based dye-sensitized solar cells, Electrochim. Acta 510 (2025) 145369, https://doi.org/10.1016/j.electacta.2024.145369.
[107] Y. Liu, Z. Wang, L. Li, S. Gao, D. Zheng, X. Yu, Q. Wu, Q. Yang, D. Zhu, W. Yang, Y. Xiong, Highly efficient quantum-dot-sensitized solar cells with composite semiconductor of ZnO nanorod and oxide inverse opal in photoanode, Electrochim. Acta 412 (2022) 140145, https://doi.org/10.1016/j.electacta.2022.140145.
[108] T.F. Yadeta, T. Imae, Effect of carbon dot on photovoltaic performance of n-TiO2/p-NiO and n-TiO2/p-CuO heterojunctions in dye-sensitized solar cells, Appl. Surf. Sci. 637 (2023), https://doi.org/10.1016/j.apsusc.2023.157880.
[109] A. Gopalraman, S. Karuppuchamy, S. Vijayaraghavan, High efficiency dye-sensitized solar cells with: v OC- J SC trade off eradication by interfacial engineering of the photoanode|electrolyte interface, RSC Adv. 9 (2019) 40292–40300, https://doi.org/10.1039/c9ra08278f.
[110] M. Ayaz, A.S. Alatawi, M. Hijji, M.A. Namazi, M.I.M. Ershath, Improving charge transfer properties and solar cell performance by In-doped TiO2 as an efficient photoanode for dye-sensitized solar cells (DSSCs), J. Phys. Chem. Solid. 188 (2024) 111913, https://doi.org/10.1016/j.jpcs.2024.111913.
[111] K.C. Rathod, K.R. Sanadi, P.D. Kamble, G.S. Kamble, M.L. Gaur, K.M. Garadkar, Photovoltaic solar application study of Cu0.5Zn0.5Se thin films by chemical Bath deposition method, Mater. Res. 25 (2022), https://doi.org/10.1590/1980-5373-MR-2021-0259.
[112] M. Radecka, M. Rekas, A. Trenczek-Zajac, K. Zakrzewska, Importance of the band gap energy and flat band potential for application of modified TiO2 photoanodes in water photolysis, J. Power Sources 181 (2008) 46–55, https://doi.org/10.1016/j.jpowsour.2007.10.082.
[113] A. Mahmood, G. Shi, Z. Wang, Z. Rao, W. Xiao, X. Xie, J. Sun, Carbon quantum dots-TiO2 nanocomposite as an efficient photocatalyst for the photodegradation of aromatic ring-containing mixed VOCs: an experimental and DFT studies of adsorption and electronic structure of the interface, J. Hazard Mater. 401 (2020) 123402, https://doi.org/10.1016/j.jhazmat.2020.123402.